Investigation of Infrared Femtosecond Laser Processing of Bulk MoS_2 at the Atomic Scale

Huimin Qi, Zongwei Xu, Jinshi Wang#, Fengzhou Fang#

State Key Laboratory of Precision measurement Technology & Instruments, Laboratory of Micro/Nano Manufacturing Technology (MNMT), Tianjin University, Tianjin, 300072, China
Corresponding Author / Email: jswang@tju.edu.cn fzfang@tju.edu.cn

KEYWORDS: Laser processing, Time-dependent density functional theory, Molybdenum disulfide, Two-dimensional materials, ACSM

Two-dimensional (2D) materials possess excellent physical and chemical properties due to their unique atomic arrangement, making them widely used in optoelectronic and energy storage devices. Currently, the patterning of 2D materials primarily relies on specific shapes of chemical vapor deposition and ion beam etching. These methods are complex and costly, and they may introduce defects and surface contamination that can affect device performance. Laser processing technology, known for its flexibility and high precision, has been widely applied in material patterning. Current research on laser processing mainly focuses on achieving monolayer removal of 2D materials through continuous laser scanning in the visible light range; however, experimental and simulation studies on infrared pulsed laser processing of bulk MoS_2 are still limited. This paper employs time-dependent density functional theory (TDDFT) for simulation, combined with experimental results, to analyze the damage threshold of bulk MoS_2 during near-threshold pulsed laser processing. The results show that the damage threshold of 8.04 nJ obtained from TDDFT is in good agreement with the experimental threshold of 32.76 nJ. The research findings provide guidance for the precise patterning of 2D materials using laser processing at the atomic scale.

NOMENCLATURE

m_e = electric mass	e = charge of electron
NA = numerical aperture	$\mathbf{E}$ = electric field
$\mathbf{A}$ = vector potential field	a.u. = atomic unit
ω = laser frequency	c = light speed
T = pulse width	I = laser intensity

1. Introduction

The discovery of two-dimensional (2D) materials, such as graphene and transition metal dichalcogenides (TMDs), has attracted significant attention due to their unique physical, chemical, and optical properties. As a widely studied TMDs, 2H-MoS_2 has a sandwich-like interlayer structure, with each unit cell containing two S-Mo-S layers. The bandgap of MoS_2 varies with the number of layers, ranging from 1.29 eV to 1.8 eV [1, 2], which covers the range of visible to near-infrared spectrum. This characteristic makes it highly suitable for photodetection fields [3]. Accurate control of the MoS_2 layer thickness is essential for optimizing photodetector performance. Although large-area, high-quality monolayer MoS_2 can be synthesized using bottom-up chemical vapor deposition (CVD) [4], the "layer + island" growth mode of multilayer MoS_2 makes is difficult to precisely control the number of layers. Therefore, top-down approaches for layer-by-layer thinning are critical for precise control of MoS_2 thickness.

Laser processing, as a highly controllable and non-contact fabrication tool, has demonstrated significant potential in the precise machining, patterning, and property modulation of 2D materials. By adjusting laser parameters such as power, pulse width, and wavelength, it is possible to achieve precise cutting, drilling, etching, and functionalization of 2D materials. Additionally, laser processing can induce phase transitions [5], doping, and defect in 2D materials, further optimizing their properties. These benefits make laser processing essential for 2D materials fabrication, widely used in electronics, photonics, and sensing devices.

Layer-by-layer thinning of MoS_2 has already been achieved using laser scanning [6, 7], which employed continuous-wave or pulsed laser. However, the removal mechanisms between laser scanning and single-point processing are different. Laser scanning introduces edge defects, which affect the absorption mechanism of laser differently from perfect lattice. Therefore, a detailed investigation of the underlying mechanisms of single-point processing is essential. This study mainly focused on the mechanisms of laser-material interaction, and presents both simulations and experimental research on laser processing of MoS_2. The damage threshold (DT) of simulations was compared with that of experimental results. These findings provide valuable insights and guidance for both laser processing of MoS_2 and MoS_2-based photodetection research.

2. Experimental approach

2.1 Simulation

This research employed time-dependent density functional theory (TDDFT) based on first-principles to study the interaction between ultrashort laser pulses and MoS_2. The simulations were performed using the OCTOPUS code [8]. Due to the periodic boundary conditions, a spatially uniform vector potential $\mathbf{A}(t)$ is employed to ensure the periodicity of the Hamiltonian. The relationship between $\mathbf{A}(t)$ and the electric field $\mathbf{E}(t)$ is as follows:

$$\mathbf{E}(t) = -\frac{1}{c}\frac{d\mathbf{A}(t)}{dt}. \quad (1)$$

Here are the parameters used in the simulation. The lattice constants for the *a*- and *b*-axis of the unit cell are 3.161 Å, with an angle of 120° between them, and the lattice constant for the *c*-axis is 12.295 Å. Real space is divided into a uniform grid with a spacing of 0.15805 Å, and **k**-space is divided into a 6 × 6 × 2 grid. The generalized gradient approximation (GGA) based on the Perdew–Burke–Ernzerhof functional (PBE) was adopted [9]. For time-dependent calculations, $\mathbf{A}(t)$ is used to represent the laser pulse, which is expressed as:

$$\mathbf{A}(t) = -c\frac{\mathbf{E}_0}{\omega}\sin^2(\frac{\pi t}{T})\cos(\omega t) \quad (0 < t < T), \quad (2)$$

where c is the speed of light, and $\mathbf{E}_0$ represents the peak electric field intensity. The relationship between $\mathbf{E}_0$ and laser intensity is: $I_0 = c|\mathbf{E}_0|^2/8\pi$. ω and T denote the laser frequency (1030 nm) and pulse width (20 fs), respectively. The approximated enforced time-reversal (AETRS) propagator with a time step Δt = 0.05 a.u. is used to perform time-dependent calculations, and total simulation time is 30 fs.

2.2 Experiments

The sample used in the experiment is a 2H-MoS_2 crystal. The surface was cleaned with tape, and a flat area was selected for the experiment. The schematic of the processing system is shown in Fig. 1. Laser pulses with a central wavelength of 1030 nm, a pulse width of 285 fs, and a repetition rate of 100 KHz, were focused onto the sample surface through an objective lens (Olympus, NA 0.75, 40 ×) after beam expansion. The surface of the sample can be observed via a CCD camera. The experiment was performed in air.

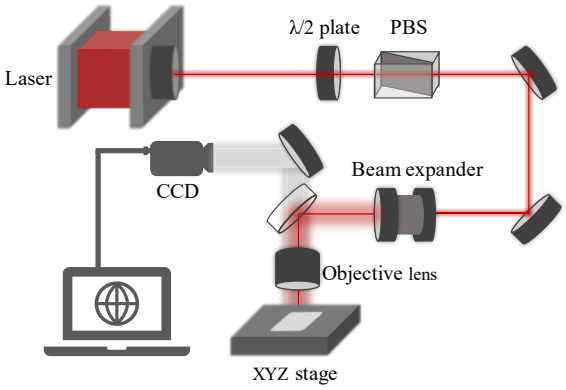

Fig. 1 Schematic diagram of femtosecond laser processing system.

3. Results and discussion

During laser irradiation, electrons in valence band absorb photons and are excited into the conduction band. As the electron density in the conduction band reaches a sufficiently high level, plasma oscillations occur in the electron gas. This process leads to a substantial transfer of laser energy to the lattice, which results in lattice damage. To have an insight into this process, the energy absorbed by the lattice (E_{ab}) and the number of excited electrons (N_{ex}) were calculated, and the results are shown in Fig. 2. In Fig. 2(a), the black squares, red circles, and blue dashed line represent E_{ab}, N_{ex}, and the reference line for two-photon absorption (TPA), respectively. As the laser intensity is below 3×10^{12} W/cm^2, the single-photon energy of the 1030 nm laser (1.204 eV) is less than the direct band gap of MoS_2 (1.5 eV) in this simulation. Therefore, the relationship between E_{ab} (or N_{ex}) with the laser intensity is E_{ab} (or N_{ex}) $\propto I^2$, which indicates that the photoionization process primarily occurs through TPA. However, as the laser intensity exceeds 3×10^{12} W/cm^2, E_{ab} and N_{ex} gradually deviate from TPA. This phenomenon can be attributed to two main reasons. First, as the laser intensity increase, the ionization mechanisms shift from predominantly TPA to tunneling ionization, which leads to the number of excited electrons to deviate from the expected values based on TPA [10]. Second, higher laser intensities excite more electrons into the conduction band. According to the Paul exclusion principle, electrons initially excited into the conduction band will preferentially occupy available states. Subsequent electrons must absorb additional photons to occupy higher orbitals. As a result, the number of excited electrons is limited [11].

Fig. 2(b) shows the N_{ex} calculated using TDDFT and Keldysh theory. The blue solid line represents the ionization rate of Keldysh [12], while the blue squares and red circles denote N_{ex} of Keldysh theory and

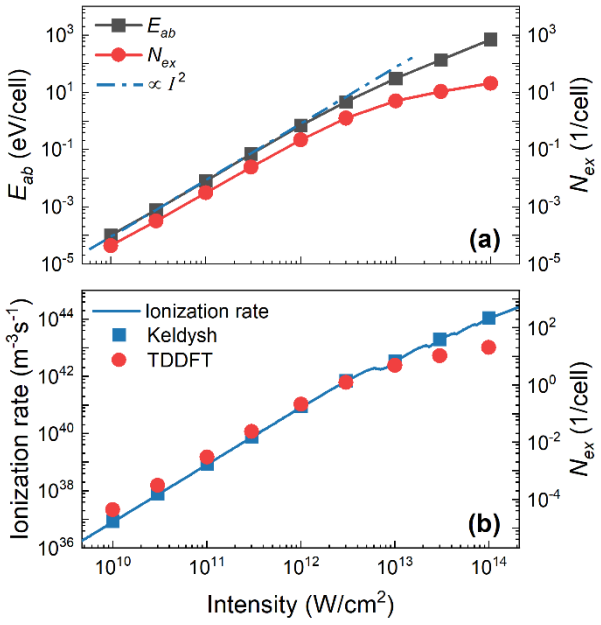

Fig. 2 Comparison between the TDDFT method and Keldysh theory. (a) The curves of E_{ab} and N_{ex} as functions of laser intensity from TDDFT simulations, with the blue dashed line representing the TAP reference line. (b) A comparison between the Nex calculated by TDDFT and that predicted by Keldysh theory. The blue solid line indicates the ionization rate derived from Keldysh ionization theory.

TDDFT simulations, respectively. At weak laser intensity, the N_{ex} of Kledysh and TDDFT both conform to TAP. However, as the laser intensity exceeds 10^{13} W/cm^2, the N_{ex} of TDDFT becomes lower than that of Keldysh, which indicates that the Pauli blocking effects suppresses N_{ex}.

The DT is a crucial physical quantity in laser processing and simulations. In TDDFT simulations, the plasma frequency method is widely used to obtain the DT, and the expression of plasma frequency is [13]:

$$\omega_p = \sqrt{\frac{4\pi n_e}{m\epsilon}}, \tag{3}$$

where n_e is the total density of conduction band electrons, and ϵ represents the dielectric constant of 2H-MoS_2 at 1030 nm laser. Electrons excited into the conduction band produce plasma oscillations. As the plasma frequency is equal to the laser frequency, a substantial amount of laser energy is transferred to the lattice, which leads to material damage. TDDFT provides the number of photoionization electrons but neglects processes such as impact ionization and electron-hole recombination. The rate equation is often used to calculate the total density of conduction electrons and is described as [14]:

$$\frac{\partial n_e(t)}{\partial t} = w_{PI}(I(t)) + w_{IM}(I(t))n_e(t) - w_R(n_e(t),t), \tag{4}$$

where w_{PI}, w_{IM}, and w_R indicate the rates of photoionization, collisional ionization, and electron relaxation resulting from defect recombination, respectively. Since the simulation involves an ideal lattice and the simulation time is significantly shorter than electrons recombination time, w_R can be ignored. w_{IM} is evaluated by [15]:

$$w_{IM} = \frac{I(t)}{\Delta}\frac{e^2}{c\epsilon nm}\frac{\tau_C}{1+\omega^2\tau_C^2}, \tag{5}$$

where Δ represents the bandgap of the 2H-MoS_2, and τ_C is the time of electron oscillation and can be expressed as:

$$\tau_C = \frac{16\pi\varepsilon^2\sqrt{m(0.1\Delta)^3}}{\sqrt{2}e^4 n_e(t)}. \tag{6}$$

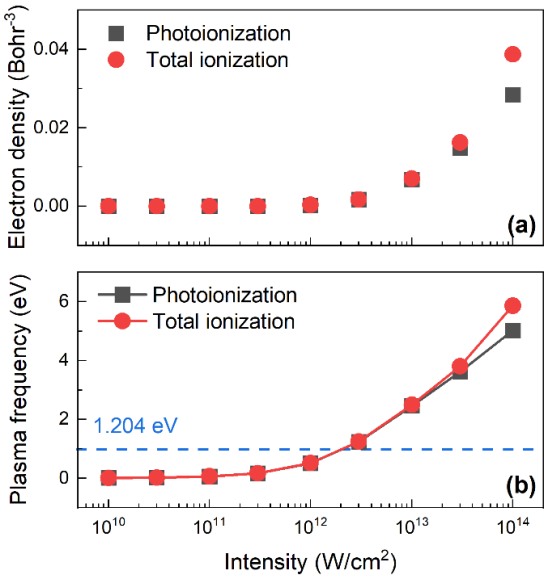

Fig. 3 The density of excited electrons for photoionization and total ionization (a) and the plasma frequency (b). In Fig3. (b), the blue dashed line represents the frequency of the 1030 nm laser (single photon energy.)

Fig. 3(a) and (b) show the N_{ex} and plasma frequency generated by photoionization and total ionization, respectively. In Fig. 3(a), at the weak field, N_{ex} generated by the two ionization methods is almost equal. However, as the laser intensity increases to 3×10^{13} W/cm^2, N_{ex} generated by total ionization is greater than that generated by ionization. In Fig. 3(b), optical breakdown occurs at 3×10^{12} W/cm^2.

The experimental results are as follows. The relationship between pulse energy (E_{pulse}) and ablation area (S) is expressed as [16]:

$$S = \frac{\pi}{2}W^2(\ln P(r_c) - \ln P_0) \tag{7}$$

where W donates the radius of the laser spot and r_c represents the radius of the ablation crater. As $S = 0$, $E_{pulse}(r_c) = E_{th}$ represents the threshold energy. S was measured using a laser confocal microscope, and the data were fitted with a straight line, as shown in Fig. 4. Based on the fitting results, W and E_{th} are 1.58 μm and 32.76 nJ, respectively. The atomic force microscopy (AFM) images of the ablation crater at low energy are shown in Fig. 5. At 40 nJ, the ablation crater exhibits smooth edges with no protrusions caused by sputtering, and the removal depth is approximately 18 nm. As the pulse energy is reduced to 38 nJ, slight accumulation of sputtered materials is observed at the edges of the ablation crater, along with the formation of a significant protrusion in the center, resulting in a depth of less than 10 nm. Further reducing the energy to 35 nJ causes rougher edges with numerous protrusions, and the removal depth decreases to about 1 nm. In addition, at the laser energy of 30 nJ, AFM measurements indicate that no material removal occurred. These experimental results also show that reducing laser energy could achieve sub-1nm precision in single-point processing.

The relationship between pulse energy and laser intensity can be expressed as:

$$E_{pulse} = \int_{-\infty}^{+\infty}\int_0^W 2\pi I_0 e^{-\frac{2r^2}{W^2}} e^{-\frac{t^2}{\tau^2}} r dr dt. \tag{8}$$

where τ is the pulse width. According to Eq.(8), the TDDFT threshold energy is 8.04 nJ, which is lower than the experimental threshold of 32.76 nJ. This discrepancy is primarily due to the different pulse widths used in the simulation and the experiment. Variations in pulse width can lead to differences in electron-phonon coupling strength, affecting the energy transfer to the lattice. However, we consider this result acceptable because they are in the same order of magnitude.

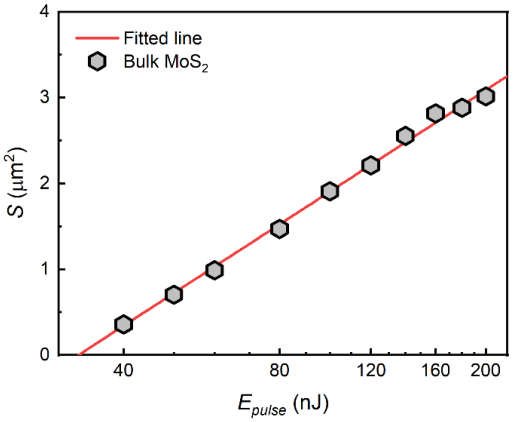

Fig. 4 The relationship between single pulse energy (E_{pulse}) and the area of ablation crater (S), with the red solid line representing the fit to the data points.

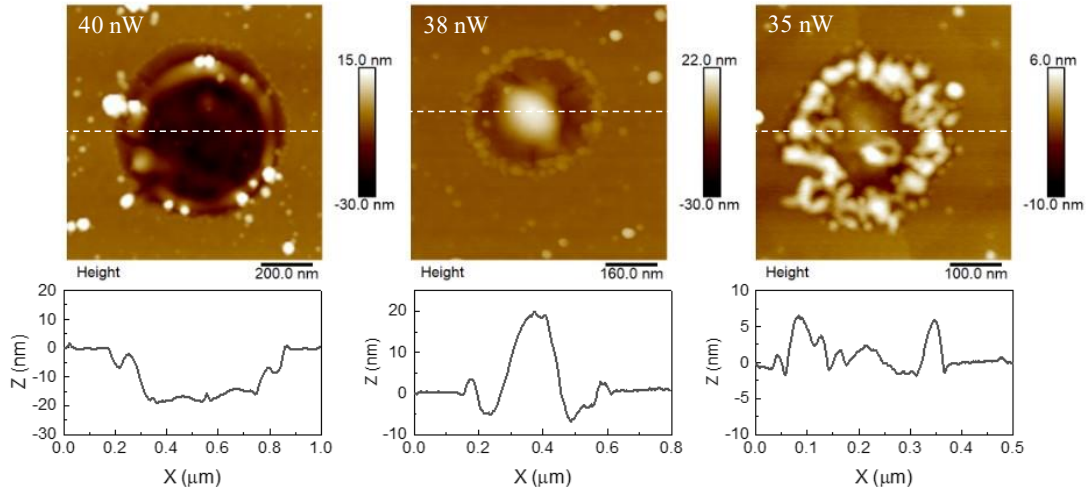

Fig. 5 AFM images of the ablation crater and the height profile along the white dashed line.

4. Conclusions

This study investigated the DT of MoS_2 under femtosecond laser irradiation using both numerical simulations and experiments. The theoretical threshold of 8.04 nJ coincides with the experimental threshold of 32.76 nJ within an acceptable margin of error. In addition, the experiments demonstrate that sub-1 nm removal of MoS_2 can be achieved through single-point laser processing. The findings are significant for near-threshold laser processing and atomic and close-to-atomic scale manufacturing (ACSM) of MoS_2 [17,18], and provide valuable insights for laser processing of other 2D materials as well.

ACKNOWLEDGEMENT

This study was supported financially by the National Natural Science Foundation (No. 52035009).

REFERENCES

1. P. C. Gu, K. L. Zhang, and Y. L. Feng *et al*., "Recent progress of two-dimensional layered molybdenum disulfide," Acta Physica Sinica, Vol. 65, No. 1, 2016.

2. A. Splendiani, L. Sun, and Y. Zhang *et al*., "Emerging Photoluminescence in Monolayer MoS_2," Nano Lett., Vol. 10, pp. 1271-1275, 2010.

3. K. S. Kim, Y. J. Ji, and K. H. Kim *et al*., "Ultrasensitive MoS_2 photodetector by serial nano-bridge multi-heterojunction," Nature Communications, Vol. 10, 2019.

4. Q. Wang, N. Li, and J. Tang *et al*., "Wafer-Scale Highly Oriented Monolayer MoS_2 with Large Domain Sizes," Nano Lett., Vol. 20, pp. 7193-7199, 2020.

5. M. X. Guan, X. B. Liu, and D. Q. Chen *et al*., "Optical Control of Multistage Phase Transition via Phonon Coupling in $MoTe_2$," Phys. Rev. Lett., Vol. 128, No. 1, 2022.

6. A. Castellanos-Gomez, M. Barkelid, and A.M. Goossens *et al*., "Laser-Thinning of MoS_2: On Demand Generation of a Single-Layer Semiconductor," Nano Lett., Vol. 12, pp. 3187-3192, 2012.

7. Y. Rho, J. Pei, and L. Wang *et al*., "Site-Selective Atomic Layer Precision Thinning of MoS_2 via Laser-Assisted Anisotropic Chemical Etching," ACS Appl. Mater. Interfaces, Vol. 11, pp. 39385-39393, 2019.

8. N. Tancogne-Dejean, M. J. T. Oliveira, and X. Andrade *et al*., "Octopus, a computational framework for exploring light-driven phenomena and quantum dynamics in extended and finite systems," J. Chem. Phys., Vol. 152, No. 12, 2020.

9. J. P. Perdew, K. Burke, and M. Ernzerhof, "Generalized Gradient Approximation Made Simple," Phys. Rev. Lett., Vol. 77, pp. 3865-3868, 1996.

10. S. L. S. B, Lokamani, and K. Ramakrishna *et al*., "Ab initio insights on the ultrafast strong-field dynamics of anatase TiO_2," Phys. Rev. B, Vol. 108, No. 19, 2023.

11. T. Apostolova and B. Obreshkov, "Femtosecond optical breakdown in silicon," Appl. Surf. Sci., Vol. 572 (2022).

12. L. V. Keldysh, "Ionization in the field of a strong electromagnetic wave." Sov. phys. JETP, Vol. 20, 1965.

13. T. Otobe, M. Yamagiwa, and J. I. Iwata *et al*., "First-principles electron dynamics simulation for optical breakdown of dielectrics under an intense laser field," Phys. Rev. B, Vol. 77, No. 16, 2008.

14. P.A. Zhokhov and A.M. Zheltikov, "Optical breakdown of solids by few-cycle laser pulses," Sci. Rep., Vol. 8, 2018.

15. V. Gruzdev, "Fundamental mechanisms of laser damage of dielectric crystals by ultrashort pulse: ionization dynamics for the Keldysh model," Opt. Eng., Vol. 53, No. 12, 2014.

16. H. An, J. Wang, and F. Fang, "Removal of SiC at atomic and close-to-atomic scale by nanosecond ultraviolet laser," Opt. Laser Technol., Vol. 158, 2023.

17. F. Fang, "The three paradigms of manufacturing advancement," J. Manuf. Syst., Vol. 63, pp. 504-505, 2022.

18. F. Fang, "Atomic and close-to-atomic scale manufacturing: perspectives and measures," Int. J. Extrem. Manuf., Vol. 2, 2020.